

Review

## Polarization Rotation and Monoclinic Distortion in Ferroelectric $(\text{Bi}_{0.5}\text{Na}_{0.5})\text{TiO}_3\text{--BaTiO}_3$ Single Crystals under Electric Fields

Motohiro Ogino <sup>1</sup>, Yuji Noguchi <sup>1,\*</sup>, Yuuki Kitanaka <sup>1</sup>, Masaru Miyayama <sup>1</sup>, Chikako Moriyoshi <sup>2</sup> and Yoshihiro Kuroiwa <sup>2</sup>

<sup>1</sup> Research Center for Advanced Science and Technology, The University of Tokyo, 4-6-1 Komaba, Meguro, Tokyo 153-8904, Japan; E-Mails: ogino@fmat.t.u-tokyo.ac.jp (M.O.); kitanaka@fmat.t.u-tokyo.ac.jp (Y.K.); miyayama@fmat.t.u-tokyo.ac.jp (M.M.)

<sup>2</sup> Graduate School of Science, Hiroshima University, 1-3-1 Kagamiyama, Higashihiroshima, Hiroshima 739-8526, Japan; E-Mails: moriyosi@sci.hiroshima-u.ac.jp (C.M.); kuroiwa@sci.hiroshima-u.ac.jp (Y.K.)

\* Author to whom correspondence should be addressed; E-Mail: yuji19700126@gmail.com; Tel./Fax: +81-3-5841-0252.

Received: 1 May 2014; in revised form: 26 June 2014 / Accepted: 27 June 2014 /

Published: 16 July 2014

**Abstract:** The features of the crystal structures and spontaneous polarization ( $P_s$ ) under an electric field ( $E$ ) have been reviewed for  $(1 - x)(\text{Bi}_{0.5}\text{Na}_{0.5})\text{TiO}_3\text{--xBaTiO}_3$  (BNT–BT). *In-situ* measurements of high-resolution synchrotron radiation X-ray diffraction (SR-XRD) under electric fields show that single crystals with  $x = 0$  (BNT) and 5% have a monoclinic distortion in space group  $Cc$  at 25 °C. The SR-XRD study combined with density functional theory (DFT) calculations demonstrates that BNT–5%BT exhibits a rotation of  $P_s$  in the monoclinic **a**–**c** plane by 2° under an  $E$  of 70 kV/cm along the <001> pseudo-cubic direction, which is much larger than BNT.

**Keywords:** ferroelectric crystals; bismuth sodium titanate; BNT; spontaneous polarization; X-ray diffraction; synchrotron radiation X-ray diffraction; DFT; monoclinic; rhombohedral

### 1. Introduction

Lead-based ferroelectric oxides of  $\text{Pb}(\text{Zr},\text{Ti})\text{O}_3$  (PZT) and related materials have been widely used for piezoelectric devices such as sensors, actuators, and nonvolatile memories. Enhanced

piezoelectric performance of relaxor-based ferroelectrics of  $\text{Pb}(\text{Zn}_{1/3}\text{Nb}_{2/3})\text{O}_3$ – $\text{PbTiO}_3$  (PZN–PT) and  $\text{Pb}(\text{Mg}_{1/3}\text{Nb}_{2/3})\text{O}_3$ – $\text{PbTiO}_3$  (PMN–PT) has attracted much attention from scientific and technological points of view. Single crystals of PZN–PT and PMN–PT exhibit an ultrahigh piezoelectric response (a strain constant  $d$  over 2500 pC/N) near morphotropic phase boundary (MPB) compositions between rhombohedral (R) and tetragonal (T) structures [1,2]. Various mechanisms have been proposed to explain the origin of the high piezoelectric response. Fu and Cohen [3] have reported the polarization rotation mechanism in which spontaneous polarization ( $P_s$ ) rotates by the application of an electric field ( $E$ ) from the  $\langle 111 \rangle_{\text{pc}}$  (pseudo-cubic notation) direction in the R phase to the  $\langle 001 \rangle$  direction in the T phase via an intermediate monoclinic (M) phase. The M phase provides a bridging pathway between the R and T phases and then the  $P_s$  vector easily rotates under a weak  $E$  [3]. It is stated that the polarization rotation is a consequence of the flat energy profile in which a small  $E$  can lead to a large change in polarization angle [3]. Lately, Damjanovic [4] has pointed out that the polarization rotation is an old concept to explain the enhanced piezoelectric properties of PZT near the MPB region and that not only the polarization rotation but also a polarization extension plays an important role in some cases in the piezoresponse of ferroelectric materials.

A growing concern regarding the toxicity in lead-containing devices and their environmental impact has, however, triggered extensive research on lead-free piezoelectric materials [5–9]. Bismuth sodium titanate ( $\text{Bi}_{0.5}\text{Na}_{0.5}\text{TiO}_3$  (BNT) has been recognized as one of the most promising candidates for the lead-free piezoelectric material [5,10–13]. To clarify the origin of its ferroelectricity, the crystal structure has been intensively analyzed in detail [14–22]. The averaged structure of BNT has been reported to be a rhombohedral structure in space group  $R\bar{3}c$ . A high resolution synchrotron radiation X-ray diffraction (SR-XRD) study reveals that BNT has a slight monoclinic distortion in the monoclinic  $Cc$  space group. The monoclinic  $Cc$  structure has been recently observed in BNT single crystals by optical birefringence microscopy [22].

Since Takenaka *et al.* [5,23–25] first reported the piezoelectric properties of  $(1-x)(\text{Bi}_{0.5}\text{Na}_{0.5})\text{TiO}_3$ – $x\text{BaTiO}_3$  (BNT–BT), polycrystalline ceramics and films of BNT–BT have been extensively studied to improve the piezoelectric performance, to investigate the phase diagram [24,26–28], the domain structure [29,30], and the relaxor behavior [31–35], and to elucidate the effect of the application of  $E$  [27,28] etc. Single crystals of BNT–BT have been grown and the influence on dc-bias  $E$  on the phase stability [36] and the diffuse X-ray scattering [37] have been investigated. Recently, a bifurcated polarization rotation model in BNT has been postulated by a neutron pair distribution analysis [38] and the piezoelectric response is suggested to originate from a polarization rotation.

Although there have been detailed studies on the crystal structures of BNT and BNT–BT [39–43], their underlying mechanism of ferroelectricity and piezoelectricity is not well understood, e.g., how the local structures near Bi and Na are developed, how the constituent ions are displaced, and how the vector of spontaneous polarization ( $P_s$ ) responds to the application of  $E$ . The study on the responses of the unit-cell parameters and atomistic polarization with respect to  $E$  are essential to clarifying the origin of the ferroelectric polarization and piezoelectric properties in the BNT system.

In this review, the intrinsic responses of unit-cell parameters, local atomic polarization and  $P_s$  to  $E$  are summarized for BNT and BNT–5%BT. The investigation of *in-situ* measurements of high-energy synchrotron radiation X-ray diffraction (SR-XRD) under an  $E$  is conducted to analyze the structural deformation by the application of  $E$ . In addition, density functional theory (DFT) calculations are used

to derive the positions in the unit cell, Born effective charges, dipole moments of the constituent atoms and therefore the  $P_s$  with respect to  $E$  is finally determined.

High-quality single crystals of BNT and BNT–5%BT grown by a high- $P_{O_2}$  (oxygen pressure) top-seeded solution growth (TSSG) method were used for the structural analyses as well as for the measurements of polarization and  $E$ -field-induced strain properties. It is emphasized that all SR-XRD data were collected under an application of  $E$ , *i.e.*, that the *in-situ* measurements of the SR-XRD under an  $E$  were conducted. To definitely distinguish the state in which an  $E$  is applied to the crystals during the measurements from the one after an electric poling, the  $E$  applied during the *in-situ* SR-XRD measurements is defined as “ $E_{in-situ}$ ”. It is demonstrated that a rotation of the  $P_s$  vector is induced by applying an  $E_{in-situ}$  for the BNT–5%BT crystals.

## 2. Experiments

Single crystals of BNT [44,45] and BNT–BT were grown at a high oxygen pressure ( $P_{O_2}$ ) of 0.9 MPa using a TSSG method [46–49]. The crystals were annealed at 950 °C for 50 h, cut into plates with a thickness of 0.2 mm. Au electrodes were sputtered onto the cut surfaces. X-ray fluorescence analysis showed that the BNT–BT crystals obtained had a composition of 0.95BNT–0.05BT (BNT–5%BT). Properties of polarization ( $P$ ) and electric-induced-strain ( $S$ ) were investigated along the  $\langle 001 \rangle_{pc}$  direction at 25 °C using the ferroelectric test system (Toyo Corporation, Tokyo, Japan, Model 6252 Rev. B). The pseudo-cubic (pc) notation is used for denoting the crystallographic axes of the pc cell.

For the SR-XRD measurements, the crystals were cut into plates with a thickness of 0.2 mm, and then gold electrodes with a thickness of 20 nm were sputtered onto the cut surfaces. The details of the SR-XRD experiments are described in the references [50,51]. The direction of  $E$ , *i.e.*, the axis normal to the crystal plates was set to be along the  $\langle 001 \rangle_{pc}$  direction. SR-XRD data were collected with a transmission geometry using a large cylindrical two-dimensional imaging plate (IP) camera with a  $1/4\chi$  three-axis goniometer at BL02B1 in the SPring-8 synchrotron radiation facility [50–53]. A high SR energy of 35 keV [wavelength: 0.035313(2) nm for BNT and 0.035345(2) nm for BNT–5%BT] was adopted so that X-rays with a high transmission ratio could penetrate through the crystals and that a high-angle diffraction pattern could be observed. The X-ray beam incident to the crystals was 150 μm in diameter. The diffraction patterns were measured in a wide  $\omega$  range of 30°–67°. The diffraction patterns were exposed on the IP camera in the following  $\Delta\omega$  of 30°–40°, 39°–49°, 48°–58°, and 57°–67°. A  $\Delta\omega$  of 1° was set to be overlapped to superimpose each of the 4 diffraction patterns.

The SR-XRD measurement temperature was kept at 25 °C, at which BNT has the monoclinic space group  $Cc$  [19,22] (see Figure 1a), where  $\mathbf{P}_s$  is approximately aligned along the  $\langle 111 \rangle_{pc}$  direction. Prior to the diffraction measurements, an  $E$  of 30–50 kV/cm, which was higher than the coercive field ( $E_c$ ) [54], was applied to the crystals along  $\langle 001 \rangle_{pc}$  as a poling treatment. To investigate the intrinsic response of the unit cell to an  $E_{in-situ}$ , SR-XRD measurements were performed at  $E_{in-situ} = 0, 30, 50, 70$ , and 100 kV/cm. During the measurements,  $E_{in-situ}$  was applied in the same  $\langle 001 \rangle_{pc}$  direction of the  $E$  in the poling treatment.

**Figure 1.** Crystal structures of BNT in the monoclinic space group (a) *Cc* and (b) *Pc* cells. The *Cc* structure in (a) is drawn from the structural parameters reported by Aksel *et al.* [19]. In this *Cc* cell, Bi and Na are randomly distributed on the A site. The monoclinic supercell in space group *Pc* [ $\text{BiNaTi}_2\text{O}_6$ ,  $Z = 4$ , see (b)], in which the structural feature in the *Cc* cell can be taken into account. In the *Pc* cell, the nearest-neighbor (NN) A-site bonds consist of five Bi–Na and one Bi–Bi or Na–Na.

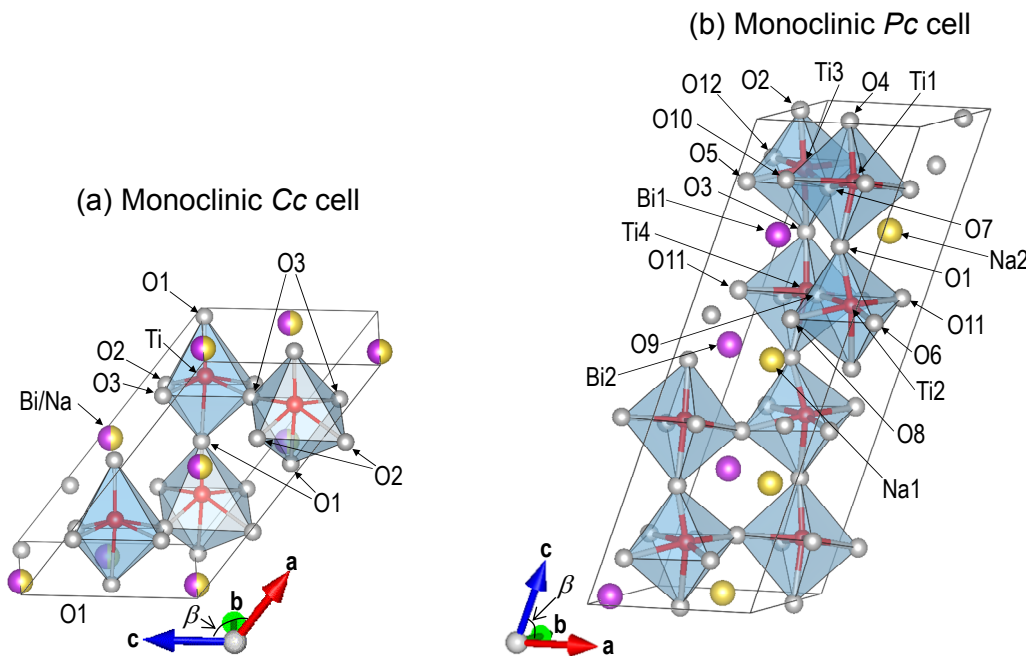
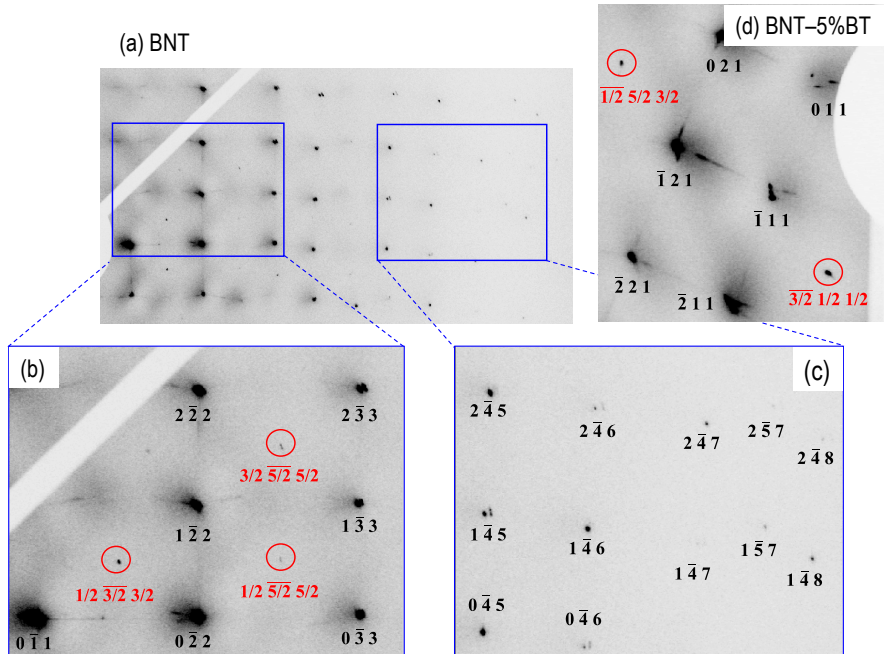


Figure 2a exhibits a diffraction pattern observed for BNT with  $E_{in-situ} = 0 \text{ kV/cm}$ . In the  $30^\circ$ – $67^\circ \omega$  range, *ca.* 880 reflections were observed in a resolution limit of the lattice spacing ( $d$ ) larger than  $0.04 \text{ nm}$  for the BNT crystals. To improve the accuracy of determining the lattice parameters *ca.* 500 reflections in the  $d$  range of  $0.055$ – $0.04 \text{ nm}$  were selected in the structure analysis. For the BNT–5%BT crystals, 660 reflections in the  $d$  range of  $0.058$ – $0.038 \text{ nm}$  were used for the analysis. The structure analysis under an application of  $E_{in-situ}$  was also conducted in a similar manner. In the SR-XRD analysis, the *C* base centered cell with the Laue class  $2/m$  was selected to determine the lattice parameters.

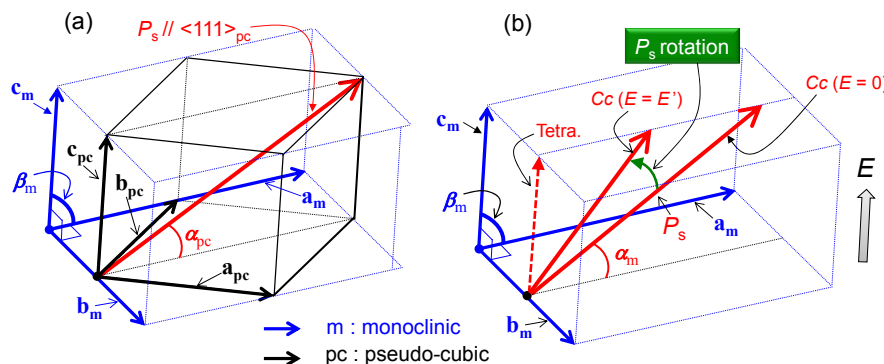
It is evident that the BNT crystals with an  $E_{in-situ}$  along the  $<001>_{pc}$  direction has a multidomain structure (the details are described in [51]). The intensity data recorded were therefore obtained as the summation of diffraction spots from each domain. The multidomain structure makes the structure analysis of the atomic positions difficult. Here, we focus our attention on the monoclinic lattice parameters as a function of  $E_{in-situ}$  applied along the  $<001>_{pc}$  direction. In the structural analysis, the diffraction spot with a higher intensity was selected in the same  $hkl$  reflections to calculate the lattice parameters. In the data in the small  $d$  range, the diffraction spots resulting from each domain were clearly separated (see Figure 4 in [51]).

**Figure 2.** Synchrotron radiation X-ray diffraction (SR-XRD) patterns at  $E_{in-situ} = 0$  kV/cm observed for the single crystals of (a–c) BNT and (d) BNT–5%BT. (b) and (c) indicate the expansions of the square parts in (a). The superlattice  $1/2$  ( $o\ o\ o$ ) reflections ( $o$ : odd) in addition to the fundamental  $hkl$  reflections from the  $\text{ABO}_3$  primitive unit cell were detected for both crystals.



The relation between the monoclinic and pc cells is depicted in Figure 3a, in which the axes of the monoclinic and pc cells are denoted by the subscript as “m” and “pc”, respectively. The monoclinic cell size used for our structure analysis is different from those of the monoclinic  $Cc$  and  $Pc$  cells. The  $C$  base centered cell with  $2/m$  symmetry can describe the crystal structures of  $Cc$  and  $Pc$  and the structural parameters can be transformed to each other.

**Figure 3.** Unit cells of pseudo-cubic (pc) and monoclinic (m) structures: (a) the relation between the pc cell and the monoclinic cell (the  $C$  base centered one with  $2/m$  symmetry) adapted for the SR-XRD analysis. In rhombohedral  $R3c$  symmetry, the  $\mathbf{P}_s$  vector is aligned along  $<111>_{pc}$  and forms an angle of  $\alpha_{pc}$  with the  $\mathbf{a}_{pc}\text{-}\mathbf{b}_{pc}$  plane. (b) depicts the schematic image of the  $\mathbf{P}_s$  rotation by applying an  $E$ . In this monoclinic cell,  $\alpha_{pc}$  is defined as the angle of the  $\mathbf{P}_s$  vector with the  $\mathbf{a}_m\text{-}\mathbf{b}_m$  plane.



### 3. Method of DFT Calculations

DFT calculations were performed to investigate the behavior of the local structure, atomic and macroscopic polarization, and their dependence on  $E_{in-situ}$  in the crystals of BNT and BNT–5%BT. The random distribution of Bi and Na on the A site leads to the averaged crystal structure in space group  $Cc$  [19] while the structure of BNT for the DFT calculations should have a lower symmetry due to an arrangement of Bi and Na [55]. We selected the monoclinic supercell in space group  $Pc$  ( $\text{BiNaTi}_2\text{O}_6$ ,  $Z = 4$ , see Figure 1b), in which the structural feature in the  $Cc$  cell can be taken into account. As for the A site atoms in the  $Pc$  cell, the nearest-neighbor (NN) A-site bonds consist of 5 Bi–Na and one Bi–Bi or Na–Na. Since the bonding of Bi–O in addition to that of Ti–O plays an important role in the ferroelectricity and piezoelectricity in the BNT system, the  $Pc$  cell in which many Bi–O–Na bonds are constructed without sacrificing the monoclinic  $Cc$  symmetry.

To determine the fractional coordinates of the constituent atoms by the DFT calculations, the lattice parameters determined by the SR-XRD analysis were employed. As described in detail below, the lattice parameters were dependent on  $E_{in-situ}$  and determined by the SR-XRD analysis with a high accuracy. The use of the lattice parameters obtained by the SR-XRD analysis in the DFT calculations enables us to investigate the influence of  $E_{in-situ}$  on the polarization ( $p_{atom}$ ) of the atoms and the resultant  $P_s$  with respect to  $E_{in-situ}$  in the crystals of BNT and BNT–5%BT in an indirect manner. In addition, similar DFT calculations were performed using the unit-cell parameters of BNT reported by Aksel *et al.* [19] for comparison.

The DFT calculations were performed with the generalized gradient approximation [56] using a plane wave basis set as implemented in the Vienna *ab-initio* simulation package (VASP). We used the projector-augmented wave potentials [57] with the valence-electron configurations of  $5d^{10}6s^26p^3$  for Bi,  $2p^63s^1$  for Na,  $3p^63d^24s^2$  for Ti, and  $2s^22p^4$  for O. The Perdew-Burke-Ernzerhof functional modified for solids (PBEsol) [58] was employed for the exchange-correlation potential. A plane-wave cut-off energy of 520 eV was adopted, and electronic energy was converged to less than  $10^{-6}$  eV in all calculations. The Monkhorst-Pack  $k$ -mesh of  $7 \times 7 \times 3$  was adopted for geometrical optimization calculations (atomic positions were relaxed with the fixed lattice parameters determined by the SR-XRD analysis). Born effective charge ( $Z^*$ ) tensors were evaluated by using a density-functional perturbation theory (DFPT) [59] for BNT with  $E_{in-situ} = 0$  kV/cm. Throughout our manuscript,  $\mathbf{P}_s$  and  $\mathbf{p}_{atom}$  denotes the vectors of spontaneous polarization and atomic polarization, respectively, and the absolute values of these vectors are defined as follows:  $P_s = |\mathbf{P}_s|$  and  $p_{atom} = |\mathbf{p}_{atom}|$ .

### 4. Results and Discussion

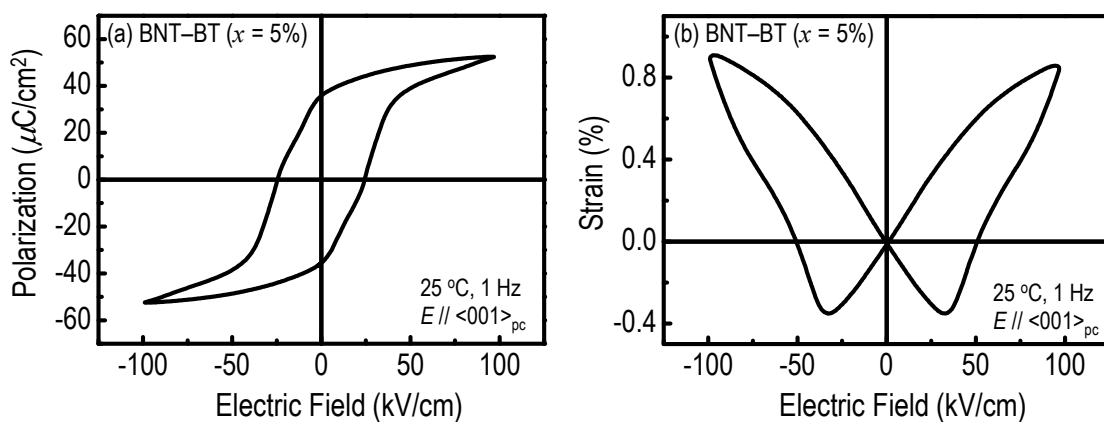
Figure 2a shows the SR-XRD pattern at  $E_{in-situ} = 0$  kV/cm observed for the single crystals of BNT. Figures 2b,c depict the expansions of the square parts in Figure 2a. In addition to the fundamental  $hkl$  reflections from the  $\text{ABO}_3$  primitive unit cell, the superlattice  $1/2$  ( $o\ o\ o$ ) reflections ( $o$ : odd) such as  $1/2\ \overline{3/2}\ 3/2$  and  $1/2\ \overline{5/2}\ 5/2$  are clearly observed. These  $1/2$  ( $o\ o\ o$ ) reflections originate from the tilting of  $\text{TiO}_6$  octahedra with  $a^- a^- a^-$  (Glazer notation [60]), which is described in the space group of rhombohedral  $R3c$  [17] or monoclinic  $Cc$  [61]. As clearly seen in Figure 2d for the BNT–5%BT crystals, apparent  $1/2$  ( $o\ o\ o$ ) reflections were observed. If the tetragonal phase in space group  $P4bm$

reported in the MPB region ( $x = 0.05\text{--}0.11$ ) [28] is present, superlattice  $1/2$  ( $o\ o\ e$ ) reflections ( $o$ : odd,  $e$ : even) should be observed, but our BNT and BNT–5%BT crystals did not exhibit any  $1/2$  ( $o\ o\ e$ ) reflection in the  $E_{in\text{-}situ}$  range of  $0\text{--}100$  kV/cm.

Figure 4a represents the polarization-electric field [ $P(E)$ ] hysteresis loop measured for the BNT–5%BT crystals along  $\langle 001 \rangle_{pc}$  at  $25^\circ\text{C}$ . The crystals exhibited a remanent polarization ( $P_r$ ) of  $36\ \mu\text{C}/\text{cm}^2$  and a coercive field ( $E_c$ ) of  $24\ \text{kV}/\text{cm}$ . This  $P_r$  is comparable to the value ( $34\ \mu\text{C}/\text{cm}^2$ ) observed for the BNT crystals along  $\langle 001 \rangle_{pc}$  [47].

Our crystals had a relatively large  $P_r$  and a small  $E_c$  compared with the reported values for other BNT–BT crystals [54,62,63]. It has been reported that the high- $P_{\text{O}_2}$  TSSG method provides high-quality crystals with low concentrations of the vacancies of Bi and O due to a suppression of the defect-formation reaction at high temperatures during the crystal-growth process [46–49]. Figure 4b shows the bipolar strain-electric field [ $S(E)$ ] curve measured for the BNT–5%BT crystals along  $\langle 001 \rangle_{pc}$  at  $25^\circ\text{C}$ .

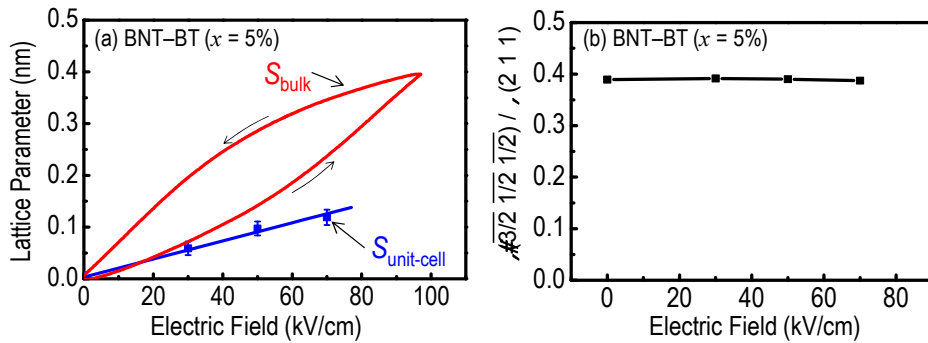
**Figure 4.** (a) Polarization-electric field [ $P(E)$ ] hysteresis loop and (b) bipolar strain-electric field [ $S(E)$ ] curve measured for the BNT–5%BT crystals along  $\langle 001 \rangle_{pc}$  at  $25^\circ\text{C}$ .



A typical butterfly curve, mainly due to a domain switching and the converse piezoelectric effect, was observed. The  $E$  at which the  $S$  had the minimum value was *ca.*  $30\ \text{kV}/\text{cm}$ , which is slightly higher than the  $E_c$  determined by the  $P(E)$  measurements. The crystals had a maximum strain ( $S_{\text{max}}$ ) up to  $0.9\%$  at an  $E$  of  $100\ \text{kV}/\text{cm}$ , which is much larger than those observed for the single crystals of BNT [64] and BNT–12%BT [46].

Figure 5a shows the unipolar strain curve ( $S_{\text{bulk}}$ ) observed for the BNT–5%BT crystals along  $\langle 001 \rangle_{pc}$ . The unit-cell strain ( $S_{\text{unit-cell}}$ ) calculated from the lattice parameter  $c_{pc}$  with respect to  $E_{in\text{-}situ}$  in the SR-XRD analysis is also plotted. The piezoelectric strain constant  $d_{33}^*$  estimated from the  $S_{\text{bulk}}$  data in the low- $E$  region ( $0\text{--}5\ \text{kV}/\text{cm}$ ) was  $138\ \text{pm}/\text{V}$ , which is comparable to the strain constant  $d_{33(\text{unit-cell})}$  of  $175(28)\ \text{pm}/\text{V}$  determined from the  $S_{\text{unit-cell}}$  data. The  $d_{33(\text{unit-cell})}$  originates from the unit-cell deformation by applying an  $E_{in\text{-}situ}$  mainly due to the intrinsic contribution, *i.e.*, the converse piezoelectric effect. In the low- $E_{in\text{-}situ}$  region below  $20\ \text{kV}/\text{cm}$ ,  $S_{\text{bulk}}$  and  $S_{\text{unit-cell}}$  are in reasonable agreement with each other. In contrast, the  $S_{\text{max}}/E_{\text{max}}$  value determined by the  $S_{\text{bulk}}$  was  $408\ \text{pm}/\text{V}$ , which is much larger than the  $d_{33}^*$  and  $d_{33(\text{unit-cell})}$  values. The hysteresis observed in the unipolar  $S_{\text{bulk}}$  curve and our SR-XRD analysis suggest that the large  $S_{\text{max}}/E_{\text{max}}$  is attributed to an extrinsic contribution by non- $180^\circ$  ferroelastic domains.

**Figure 5.** (a) Unipolar strain curve ( $S_{\text{bulk}}$ ) observed for the BNT–5%BT crystals along  $<001>_{\text{pc}}$  at 25 °C. The unit-cell strain ( $S_{\text{unit-cell}}$ ) calculated from the lattice parameter  $c_{\text{pc}}$  with respect to  $E_{\text{in-situ}}$  determined in the SR-XRD analysis is also plotted. Figure (b) represents the intensity ( $I$ ) ratio of superlattice  $\overline{3}/2 \overline{1}/2 1/2$  reflection to fundamental  $\overline{2} \overline{1} 1$  one as a function of  $E_{\text{in-situ}}$  applied along  $<001>_{\text{pc}}$  for the BNT–5%BT crystals.



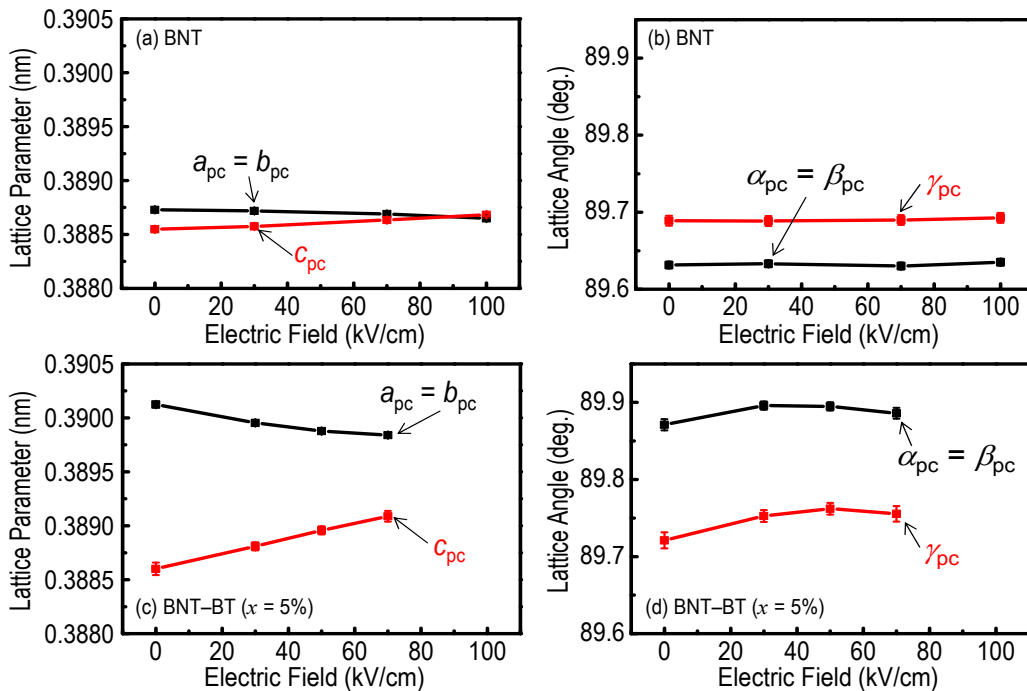
When an  $E_{\text{in-situ}}$  is applied along  $<001>_{\text{pc}}$  to R(or M) crystals with  $\mathbf{P}_s$  mainly along  $<111>_{\text{pc}}$ , an  $E$ -induced phase transition from the R(or M) to a T phase is expected, as observed for PZN–PT and PMN–PT crystals [3]. Such an  $E$ -induced phase transition should change the intensity of the  $1/2$  ( $o\ o\ o$ ) reflections with respect to the fundamental  $hkl$  ones. Figure 5b represents the intensity of the  $\overline{3}/2 \overline{1}/2 1/2$  superlattice spot as a function of  $E_{\text{in-situ}}$  observed for the BNT–5%BT crystals. The intensity of  $\overline{3}/2 \overline{1}/2 1/2$  normalized by the fundamental spot of  $\overline{2} \overline{1} 1$  exhibits no change by applying an  $E_{\text{in-situ}}$  up to 70 kV/cm. These results clearly show that the BNT–5%BT crystals do not undergo any  $E$ -induced phase transition and that they remain as the monoclinic  $Cc$  (described in detail below).

Figure 6 shows the pc unit cell parameters as a function of  $E_{\text{in-situ}}$  along  $<001>_{\text{pc}}$ . The rhombohedral  $R3c$  cell has the relations of  $a_{\text{pc}} = b_{\text{pc}} = c_{\text{pc}}$  and  $\alpha_{\text{pc}} = \beta_{\text{pc}} = \gamma_{\text{pc}}$ , but both the crystals of BNT and BNT–5%BT exhibit a structural deviation from the  $R3c$  cell. These results are direct evidence that the BNT and BNT–5%BT crystals have monoclinic  $Cc$  symmetry.

With increasing  $E_{\text{in-situ}}$ ,  $a_{\text{pc}}$  was compressed while  $c_{\text{pc}}$  was elongated mainly due to the converse piezoelectric effect. For the BNT crystals,  $\alpha_{\text{pc}}$  and  $\gamma_{\text{pc}}$  remained constant around 89.63° and 89.69°, respectively, regardless of  $E_{\text{in-situ}}$ . It is worth noting that the BNT–5%BT crystals presented increasing trends of  $\alpha_{\text{pc}}$  and  $\gamma_{\text{pc}}$  with  $E_{\text{in-situ}}$ . In particular,  $\gamma_{\text{pc}}$  markedly increased by 0.04° by  $E_{\text{in-situ}}$ , which is much larger than the detection limit of 0.005°–0.007°.

Ma *et al.* [27] have reported that BNT ceramics exhibited an  $E$ -induced phase transition from the  $Cc$  to  $R3c$  phase at a poling  $E$  of *ca.* 50 kV/cm. It is interesting to note that the transition is found to be irreversible, *i.e.*, that the  $R3c$  phase is shown to be maintained in the ceramics without the application of  $E$ . This is quite different from the  $E$ -induced phase transitions reported for BaTiO<sub>3</sub>-based [65–67] and PbTiO<sub>3</sub>-based [2,68–71] single crystals. Considering the fact that the BNT single crystals did not exhibit any change in crystal symmetry, the  $Cc$ - $R3c$  phase transition induced by the poling is considered peculiar only for the ceramic forms in the BNT system.

**Figure 6.** Pseudo-cubic (pc) unit-cell parameters as a function of  $E_{in-situ}$  along  $\langle 001 \rangle_{pc}$ : (a) lattice parameters and (b) lattice angel observed for the BNT crystals, (c) lattice parameters and (d) lattice angel observed for the BNT–5%BT crystals.



The bond lengths obtained by the DFT calculations by employing the lattice parameters at  $E_{in-situ} = 0$  kV/cm are listed in Tables 1–3. The absolute values of the bond length are quite similar for BNT(Aksel *et al.* [19]), BNT, and BNT–5%BT and their differences are as small as 0.8% at most. With respect to the cages composed of O atoms, Ti and Bi display an averaged displacement along  $\langle 111 \rangle_{pc}$ , which results in short and long bonding characteristics. For the Ti–O bonding, the three short bonds with 0.181–0.195 nm are seen, which leads to three long bonds with 0.20–0.22 nm. The bond valence sum (BVS) [72] of Ti is calculated to be 3.95–4.05, which accords well with the nominal ionic valence of  $Ti^{4+}$ . It is interesting to note that Bi exhibits an enhanced off-centering with respect to the cage of twelve O atoms approximately along the **c** axis in the *Pc* cell (Figure 1b). These large displacements of Bi cause a considerable difference between the short and long Bi–O bonds. The short Bi–O bonds are in the range of 0.22–0.25 nm while the long Bi–O bonds are found in 0.30–0.33 nm. The averaged short and long bonds of Bi–O are quantitatively in good agreement with 0.22 nm and 0.32 nm determined by the neutron pair distribution analysis [38]. The short bond of Bi–O also accords with 0.22 nm estimated by the extended X-ray absorption fine structure studies [73]. The BVS of Bi is estimated to be 3.14–3.16, which is slightly larger than the nominal ionic valence of  $Bi^{3+}$ . For the Na–O bonding, the short and long bonds are formed, whereas the off-centering of Na is not significant compared with that of Bi due to the ionic nature of Na atoms. Actually, the BVS of Na is *ca.* 1.1, which is almost the same as that of the nominal formal valence of  $Na^+$ .

**Table 1.** Bond lengths of Ti–O obtained by the density functional theory (DFT) calculations for BNT and BNT–5%BT with  $E_{in-situ} = 0$  kV/cm in the  $Pc$  cell.

Bond length (nm)	BNT <sup>b</sup>	BNT ( $E_{in-situ} = 0$ kV/cm)	BNT–5%BT ( $E_{in-situ} = 0$ kV/cm)
Ti1–O12	0.1812	0.1813	0.1812
Ti1–O5	0.1861	0.1864	0.1863
Ti1–O4	0.1894	0.1893	0.1900
Ti1–O1	0.2069	0.2085	0.2080
Ti1–O10	0.2120	0.2116	0.2133
Ti1–O7	0.2179	0.2178	0.2193
BVS <sup>a</sup>	4.02	3.99	3.95
Ti2–O11	0.1869	0.1876	0.1874
Ti2–O6	0.1875	0.1880	0.1882
Ti2–O1	0.1905	0.1904	0.1915
Ti2–O2	0.2048	0.2069	0.2064
Ti2–O8	0.2075	0.2072	0.2083
Ti2–O9	0.2076	0.2071	0.2082
BVS <sup>a</sup>	4.02	3.98	3.93
Ti3–O2	0.1859	0.1856	0.1859
Ti3–O7	0.1906	0.1908	0.1909
Ti3–O10	0.1945	0.1953	0.1954
Ti3–O5	0.2006	0.2005	0.2014
Ti3–O12	0.2020	0.2022	0.2030
Ti3–O3	0.2069	0.2089	0.2087
BVS <sup>a</sup>	4.05	4.01	3.97
Ti4–O3	0.1848	0.1845	0.1847
Ti4–O8	0.1851	0.1854	0.1851
Ti4–O9	0.1869	0.1871	0.1870
Ti4–O6	0.2102	0.2104	0.2118
Ti4–O4	0.2117	0.2136	0.2133
Ti4–O11	0.2128	0.2125	0.2145
BVS <sup>a</sup>	4.02	3.99	3.96

<sup>a</sup> Bond valence sum (BVS) (see text); <sup>b</sup> The lattice parameters in the monoclinic  $Cc$  structure reported by Aksel *et al.* [19] are employed.

Table 4 lists the  $Z^*$  tensors of the constituent atoms obtained for the  $Pc$  cell calculated using the unit-cell parameters of BNT ( $E_{in-situ} = 0$  kV/cm). The  $Z^*$  tensors reflects the relations expected from symmetry, as reported for monoclinic  $ZrO_2$  [74]. In the  $Pc$  cell, as all of the constituent atoms are on the  $2a$  site, an atom at  $(x, y, z)$  and its partner atom at  $(x, -y, z + 1/2)$  are structurally equivalent. For the atoms on the same  $2a$  site, the absolute values of the matrix elements are the same. The off-diagonal matrix elements of  $xy$ ,  $yx$ ,  $yz$  and  $zy$  change sign between the partners while those of  $xz$  and  $zx$  and the diagonal matrix elements of  $xx$ ,  $yy$  and  $zz$  have the same sign.

**Table 2.** Bond lengths of Bi–O obtained by the DFT calculations for BNT and BNT–5%BT with  $E_{in-situ} = 0$  kV/cm in the  $Pc$  cell.

Bond length (nm)	BNT <sup>b</sup>	BNT ( $E_{in-situ} = 0$ kV/cm)	BNT–5%BT ( $E_{in-situ} = 0$ kV/cm)
Bi1–O7	0.2271	0.2274	0.2270
Bi1–O1	0.2298	0.2302	0.2293
Bi1–O10	0.2358	0.2349	0.2352
Bi1–O9	0.2403	0.2422	0.2426
Bi1–O3	0.2457	0.2461	0.2473
Bi1–O5	0.2472	0.2473	0.2495
Bi1–O8	0.3074	0.3095	0.3100
Bi1–O3	0.3082	0.3096	0.3107
Bi1–O12	0.3120	0.3120	0.3135
Bi1–O11	0.3199	0.3208	0.3207
Bi1–O6	0.3245	0.3252	0.3252
Bi1–O1	0.3298	0.3277	0.3302
BVS <sup>a</sup>	3.16	3.13	3.10
Bi2–O4	0.2277	0.2277	0.2270
Bi2–O6	0.2332	0.2329	0.2327
Bi2–O11	0.2355	0.2350	0.2354
Bi2–O2	0.2419	0.2431	0.2444
Bi2–O10	0.2433	0.2451	0.2452
Bi2–O8	0.2464	0.2470	0.2490
Bi2–O7	0.3064	0.3084	0.3078
Bi2–O9	0.3089	0.3102	0.3123
Bi2–O2	0.3109	0.3118	0.3128
Bi2–O5	0.3134	0.3139	0.3138
Bi2–O12	0.3152	0.3158	0.3160
Bi2–O4	0.3316	0.3298	0.3321
BVS <sup>a</sup>	3.14	3.10	3.07

<sup>a</sup> Bond valence sum (BVS) (see text); <sup>b</sup> The lattice parameters in the monoclinic  $Cc$  structure reported by Aksel *et al.* [19] are employed.

In  $Pc$  space group,  $\mathbf{P}_s$  lies in the  $\mathbf{a}$ – $\mathbf{c}$  plane and contains  $x$  and  $z$  components, which emphasizes the importance of the  $xx$  and  $zz$  elements of the  $Z^*$  tensors. It is worth noting that the  $xx$  and  $zz$  elements are quite different from the nominal ionic charges of  $\text{Bi}^{3+}$ ,  $\text{Ti}^{4+}$ , and  $\text{O}^{2-}$  whereas only Na exhibits the similar value expected from that of  $\text{Na}^+$ . The large  $Z^*$  is considered as a result of a strong dynamic charge transfer between Bi–O and Ti–O. The  $Z^*$  much larger than the nominal ionic charge reflects the delocalized structure of the electronic charge distributions, which is quite common in other ferroelectric perovskite oxides [74,75].

Considering the relations between the  $Z^*$  tensors and the bond lengths, we find the characteristic feature of the large effective charge elements caused by the dynamic charge transfer. The  $zz$  elements in the  $Z^*$  tensors of O1–O4 are extraordinarily large compared with other elements whereas other O atoms except for O10 exhibit the  $zz$  elements close to the nominal ionic valence (−2). The quite large  $zz$  elements of O1–O4 are a result of the dynamic charge transfer due to the formation of the short

bonds of Ti1–O4, Ti2–O1, Ti3–O2, and Ti4–O3, which are approximately normal to the **a**–**b** plane in the *Pc* cell. As for the  $Z^*$  tensors of O5–O12, the  $xx$  and  $yy$  elements are relatively large compared with their  $zz$  elements, which is attributed to the formation of the short bonds between Ti and O parallel to the **a**–**b** plane. These short Ti–O bonds form an angle of *ca.* 45° with the **a** and **b** axes, which enlarges both the  $xx$  and  $zz$  elements. The relatively large  $zz$  element of O10 results from the formation of the short bonds with Bi1 and Bi2 that are aligned averagely along the **c** axis.

**Table 3.** Bond lengths of Na–O obtained by the DFT calculations for BNT and BNT–5%BT with  $E_{in-situ} = 0$  kV/cm in the *Pc* cell.

Bond length (nm)	BNT <sup>b</sup>	BNT ( $E_{in-situ} = 0$ kV/cm)	BNT–5%BT ( $E_{in-situ} = 0$ kV/cm)
Na1–O4	0.2423	0.2439	0.2454
Na1–O12	0.2430	0.2451	0.2463
Na1–O6	0.2447	0.2456	0.2479
Na1–O8	0.2508	0.2516	0.2519
Na1–O9	0.2510	0.2515	0.2518
Na1–O2	0.2582	0.2589	0.2590
Na1–O2	0.2997	0.2974	0.2990
Na1–O11	0.3065	0.3061	0.3072
Na1–O5	0.3071	0.3093	0.3095
Na1–O4	0.3108	0.3109	0.3116
Na1–O10	0.3124	0.3129	0.3128
Na1–O7	0.3178	0.3178	0.3177
BVS <sup>a</sup>	1.14	1.11	1.09
Na2–O1	0.2432	0.2446	0.2461
Na2–O7	0.2434	0.2442	0.2465
Na2–O11	0.2434	0.2454	0.2465
Na2–O5	0.2530	0.2539	0.2542
Na2–O12	0.2554	0.2559	0.2560
Na2–O3	0.2565	0.2568	0.2577
Na2–O3	0.3023	0.3003	0.3011
Na2–O9	0.3026	0.3022	0.3016
Na2–O8	0.3058	0.3052	0.3046
Na2–O6	0.3081	0.3088	0.3089
Na2–O1	0.3084	0.3087	0.3096
Na2–O10	0.3096	0.3108	0.3123
BUS <sup>a</sup>	1.14	1.11	1.08

<sup>a</sup> Bond valence sum (BVS) (see text); <sup>b</sup> The lattice parameters in the monoclinic *Cc* structure reported by Aksel *et al.* [19] are employed.

**Table 4.** Born effective charge ( $Z^*$ ) tensors of the constituent atoms obtained for the  $Pc$  cell calculated using the unit-cell parameters of BNT ( $E_{in-situ} = 0$  kV/cm). The elements in the  $Z^*$  tensors are listed below.

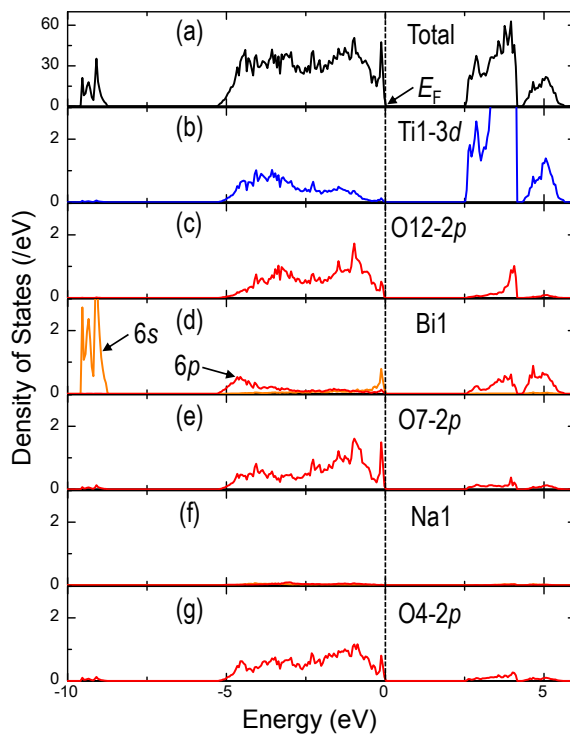
Atom	$xx$	$yy$	$zz$	$xy$	$xz$	$yx$	$yz$	$zx$	$zy$
Bi1	4.18	5.05	5.03	0.29	-0.64	-0.35	0.31	-0.41	-0.33
Bi2	4.41	5.08	5.09	0.28	-0.44	-0.24	0.33	-0.66	-0.37
Na1	1.17	1.18	1.11	-0.03	0.02	0.02	-0.04	-0.03	0.03
Na2	1.19	1.20	1.14	-0.02	-0.03	0.03	-0.02	0.04	0.04
Ti1	6.58	5.29	5.77	0.33	-0.78	-0.10	0.67	-0.44	-0.38
Ti2	5.42	7.21	6.48	-0.36	-0.98	0.34	-0.51	-1.38	0.54
Ti3	5.07	8.13	6.62	-0.07	-0.37	0.52	0.08	-0.49	0.10
Ti4	6.03	6.05	5.97	-0.02	-0.08	0.00	0.08	0.07	0.06
O1	-2.77	-1.32	-5.02	0.02	0.46	-0.16	-0.17	0.59	-0.24
O2	-1.15	-2.90	-5.44	0.23	-0.06	0.10	0.30	0.04	0.56
O3	-1.27	-2.88	-5.22	0.11	0.36	0.09	0.36	0.17	0.51
O4	-3.02	-1.25	-4.69	0.08	0.87	-0.09	-0.22	0.60	-0.24
O6	-3.31	-3.91	-2.08	-1.46	-0.10	-1.49	0.96	-0.14	0.73
O7	-2.96	-3.70	-2.14	-1.22	0.06	-1.27	0.81	0.16	0.76
O9	-2.89	-4.08	-2.19	-1.49	0.32	-1.59	-0.66	0.59	-0.55
O10	-2.76	-3.98	-2.97	1.26	0.09	1.10	-0.01	0.07	0.09
O11	-2.99	-4.06	-2.17	1.54	-0.29	1.44	-0.55	-0.34	-0.73
O12	-3.37	-3.96	-1.42	-2.05	-0.05	-2.15	-0.07	0.05	0.17

The charge transfer feature can be evaluated by electronic density of states (DOS). If Ti atoms have the nominal ionic valence of +4, the electronic configuration of  $Ti^{4+}$  is expressed as [Ar]3d<sup>0</sup> and should not possess partial DOS (PDOS) in the valence band (VB). Similarly,  $Bi^{3+}$  with 6s<sup>2</sup>6p<sup>0</sup> does not have PDOS in the VB if Bi atoms behave as an ion with the nominal valence of +3. Figure 7 exhibits the (a) total DOS and (b)–(g) PDOS of the representative constituent atoms of BNT ( $E_{in-situ} = 0$  kV/cm). In these plot, the valence band maximum (VBM) is set to be the Fermi level, *i.e.*, 0 eV. As reported for BaTiO<sub>3</sub> and PbTiO<sub>3</sub> [76,77], the PDOS of the Ti-3d states are found in the valence band (VB, -5 to 0 eV) due to the dynamic charge transfer, *i.e.*, the orbital hybridization between the 3d states of Ti and the 2p states of the neighboring O forming the short bonds with Ti. It is interesting to note that Bi has some PDOS of 6p in the VB resulting from the Bi-6p-O-2p hybridization, which is similar to the Pb-6p-O-2p one reported for PbTiO<sub>3</sub> [78]. In contrast, Na has almost no PDOS in the VB, showing that Na has an ionic nature in BNT. This result is consistent with the calculation of the  $Z^*$  tensor of Na. The orbital hybridizations of Bi and Ti with O lower the energy levels with occupied electrons, leading to the characteristic short bonds, as listed in Tables 1–3.

Table 5 lists the structural parameters obtained by the DFT calculations for BNT ( $E_{in-situ} = 0$  kV/cm). The displacements of atoms along the **a** ( $\Delta x$ ) and **c** ( $\Delta z$ ) axes in the  $Pc$  cell are estimated from the center of the polyhedral cages. For example, the center of a TiO<sub>6</sub> octahedron is determined to be the position at which the sum of the displacements of the six O atoms becomes zero both along the **a** and **c** axes. Using these displacements and the  $Z^*$  tensors, the *x* ( $p_a$ ) and *z* ( $p_c$ ) components of  $\mathbf{p}_{atom}$  are obtained as a dipole moment per the unit-cell volume. The angle of  $\mathbf{p}_{atom}$  with the **a**–**b** plane is defined as  $\alpha p_{atom}$ , which is obtained by the  $p_a$ ,  $p_c$ , and the monoclinic angle  $\beta$ . The direction of  $\alpha p_{atom}$  is

expressed by  $[uvw]$ , as listed in Table 5, where  $[uvw]$  is calculated to be  $[11\bar{v}]$  in the pc cell. As the sum values of  $p_a$  and  $p_c$  are denoted as  $P_a$  and  $P_c$ , respectively,  $P_a = 35.8 \mu\text{C}/\text{cm}^2$  and  $P_c = 41.9 \mu\text{C}/\text{cm}^2$  are obtained. To estimate the contributions of Bi, Na, Ti, and O to the macroscopic polarization, the polarization vectors of Bi, Na, Ti, and O are calculated and the results are as follows:  $p_{\text{Bi}} = 28.2 \mu\text{C}/\text{cm}^2$  ( $\alpha_m = 35.6^\circ$ ),  $p_{\text{Na}} = 5.3 \mu\text{C}/\text{cm}^2$  ( $\alpha_m = 36.8^\circ$ ),  $p_{\text{Ti}} = 34.5 \mu\text{C}/\text{cm}^2$  ( $\alpha_m = 36.8^\circ$ ), and  $p_{\text{O}} = -4.8 \mu\text{C}/\text{cm}^2$  ( $\alpha_m = -11.0^\circ$ ). The summation of these  $p$  vectors leads to a  $P_s$  of  $63.7 \mu\text{C}/\text{cm}^2$  with its angle ( $\alpha_m$ ) of  $38.2^\circ$  with the  $\mathbf{a}-\mathbf{b}$  plane. Table 6 lists the structural parameters obtained by the DFT calculations for BNT–5%BT ( $E_{\text{in-situ}} = 0 \text{ kV}/\text{cm}$ ) in the same manner, and  $P_a = 38.6 \mu\text{C}/\text{cm}^2$  and  $P_c = 40.4 \mu\text{C}/\text{cm}^2$  are obtained.

**Figure 7.** (a) Total and (b–g) partial density of states (DOS) of the representative constituent atoms of BNT ( $E_{\text{in-situ}} = 0 \text{ kV}/\text{cm}$ ) obtained by the DFT calculations in which the  $Pc$  cell with its fixed lattice parameters determined by the SR-XRD analysis is adapted. The valence band maximum (VBM) is set to be the Fermi level, *i.e.*,  $0 \text{ eV}$ .



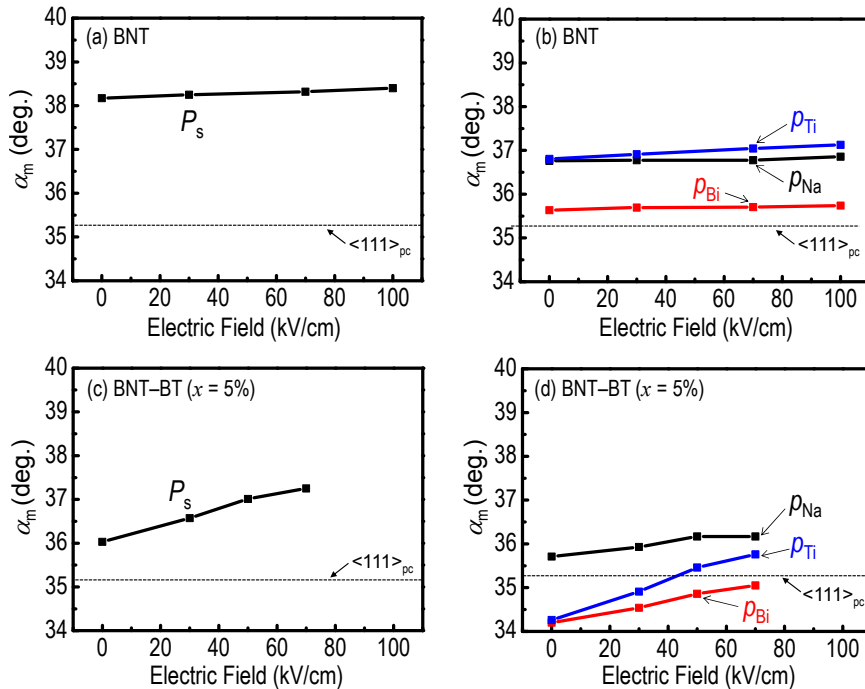
The  $P_s$  of BNT is found to be  $63.7 \mu\text{C}/\text{cm}^2$ , which leads to a  $\langle 001 \rangle_{\text{pc}}$  component of  $39.4 \mu\text{C}/\text{cm}^2$ . This agrees well with the  $P_r$  ( $34 \mu\text{C}/\text{cm}^2$ ) observed for the BNT crystals along  $\langle 001 \rangle_{\text{pc}}$  [47]. The angle ( $\alpha_m$ ) of  $\mathbf{P}_s$  with the  $\mathbf{a}_m-\mathbf{b}_m$  plane (Figure 3b) is estimated to be  $38.2^\circ$ , which is slightly higher than the  $\langle 111 \rangle_{\text{pc}}$  angle ( $\alpha_{\text{pc}}$ ) of  $35.3^\circ$  (Figure 3a). This result shows that the crystal structure of BNT is well described by the rhombohedral  $R3c$  symmetry [38]. The  $P_s$  of BNT–5%BT is obtained to be  $64.6 \mu\text{C}/\text{cm}^2$ , which results in a  $\langle 001 \rangle_{\text{pc}}$  component of  $38.0 \mu\text{C}/\text{cm}^2$ . This  $P_s$  component accords qualitatively with the  $P_r$  of  $36 \mu\text{C}/\text{cm}^2$  observed for the BNT–5%BT crystals along  $\langle 001 \rangle_{\text{pc}}$ .

Figure 8 exhibits the  $\alpha_m$  of  $\mathbf{P}_s$  and  $\mathbf{p}_{\text{atom}}$  as a function of  $E_{\text{in-situ}}$ . The DFT calculations in the  $Pc$  cell were conducted using the lattice parameters determined by the SR-XRD analysis (see Figure 6) to incorporate the influence of  $E_{\text{in-situ}}$  on  $\mathbf{P}_s$  and  $\mathbf{p}_{\text{atom}}$ . The values of  $P_s$  and  $p_{\text{atom}}$  did not depend on  $E_{\text{in-situ}}$ .

and the difference in  $p_{\text{atom}}$  caused by the application of  $E_{\text{in-situ}}$  was less than  $0.1 \mu\text{C}/\text{cm}^2$  for both BNT and BNT–5%BT. It is interesting to note that  $\alpha_m$  displays a characteristic trend with  $E_{\text{in-situ}}$ . BNT is found to show an almost constant  $\alpha_m$  of around  $38.2^\circ$  and the rotation angle ( $\Delta\alpha_m$ ) of  $\mathbf{P}_s$  by  $E_{\text{in-situ}}$  was as small as  $0.2^\circ$ , which is due to the constant lattice parameters of BNT regardless of  $E_{\text{in-situ}}$ . Note that the  $\alpha_m$  of BNT–5%BT varies significantly from  $36.0^\circ$  ( $E_{\text{in-situ}} = 0 \text{ kV/cm}$ ) to  $37.3^\circ$  ( $E_{\text{in-situ}} = 70 \text{ kV/cm}$ ) and that its  $\Delta\alpha_m$  reaches  $1.3^\circ$ . These results clearly show that BNT–5%BT features an electrically soft with respect to the rotation of  $\mathbf{P}_s$  by  $E_{\text{in-situ}}$ .

One of the possible origins of the  $\mathbf{P}_s$  rotation observed for the BNT–5%BT crystals is that this composition is present near the MPB between monoclinic  $Cc$  and tetragonal  $P4bm$ . Transmission electron microscopy observations by Ma *et al.* [28] have revealed that  $(1 - x)\text{BNT}-x\text{BT}$  ceramics without an application of  $E$  exhibit  $P4bm$  symmetry in the  $x$  range of 6%–10%. Neutron powder diffraction study conducted by Kitanaka *et al.* [79] have reported direct evidence of tetragonal  $P4bm$  for BNT–7%BT powder. The  $P4bm$  phase has a  $\mathbf{P}_s$  of  $4 \mu\text{C}/\text{cm}^2$  [79] along  $\langle 001 \rangle_{\text{pc}}$ , as depicted in Figure 3b. It is suggested that the MPB between monoclinic  $Cc$  and tetragonal  $P4bm$  lies around  $x$  of 6%. This implies that the  $Cc$  and  $P4bm$  phases are energetically competitive but that an energy barrier for the  $E$ -induced phase transition from the  $Cc$  to  $P4bm$  phase is not overcome in the BNT–5%BT crystals under an  $E_{\text{in-situ}}$  along  $\langle 001 \rangle_{\text{pc}}$  up to  $70 \text{ kV/cm}$ . Although the application of  $E_{\text{in-situ}}$  does not lead to a phase transition, the  $\mathbf{P}_s$  rotation observed is considered as a sign of the  $E$ -induced phase transition. A materials design for enhancing piezoelectric response of Bi-based ferroelectric oxides based on the  $\mathbf{P}_s$  rotation is expected to be developed by the studies of the structural analyses under  $E_{\text{in-situ}}$  combined with DFT calculations.

**Figure 8.** Angles ( $\alpha_m$ ) of the (a,c)  $\mathbf{P}_s$  and (b,d)  $\mathbf{p}_{\text{atom}}$  vectors as a function of  $E_{\text{in-situ}}$  along  $\langle 001 \rangle_{\text{pc}}$ . The  $\alpha_m$  is defined as the angle of  $\mathbf{P}_s$  or  $\mathbf{p}_{\text{atom}}$  with the  $\mathbf{a}_m-\mathbf{b}_m$  plane.  $P_s$  and  $p_{\text{atom}}$  denotes  $P_s = |\mathbf{P}_s|$  and  $p_{\text{atom}} = |\mathbf{p}_{\text{atom}}|$ .  $\mathbf{P}_s$  and  $\mathbf{p}_{\text{atom}}$  are estimated from the off-center displacements and the Born effective charge ( $Z^*$ ) tensors obtained by the DFT calculations.



**Table 5.** Structural parameters obtained by the DFT calculations for BNT ( $E_{in-situ} = 0$  kV/cm) in the  $Pc$  cell. The following lattice parameters were used:  $a = 0.55124$  nm,  $b = 0.54825$  nm,  $c = 1.65376$  nm,  $\alpha = \gamma = 90.0000^\circ$ , and  $\beta = 70.0105^\circ$ . The  $P_s$  of  $63.7\text{ }\mu\text{C}/\text{cm}^2$  with its angle ( $\alpha_m$ ) of  $38.2^\circ$  is estimated.

Atom	x (-)	y (-)	z (-)	$\Delta x$ (nm) <sup>a</sup>	$\Delta z$ (nm) <sup>a</sup>	$p_a$ <sup>b</sup> ( $\mu\text{C}/\text{cm}^2$ )	$p_c$ <sup>b</sup> ( $\mu\text{C}/\text{cm}^2$ )	$\alpha p_{atom}$ <sup>c</sup> (deg)	[u]	u	v] <sup>d</sup>
Bi1	0.2726	0.7478	0.2566	0.03296	0.02772	8.24	8.64	35.96	1	1	1.03
Bi2	0.0203	0.2544	0.0077	0.03172	0.02944	8.71	8.85	35.32	1	1	1.00
Na1	0.4986	0.7498	0.0034	0.01976	0.02231	1.63	1.66	35.36	1	1	1.00
Na2	0.7470	0.2538	0.2529	0.01885	0.02162	1.48	1.74	38.19	1	1	1.11
Ti1	0.6218	0.7584	0.3732	0.01876	0.01381	7.73	4.90	26.08	1	1	0.69
Ti2	0.8627	0.7524	0.1224	0.01371	0.01237	4.27	4.20	34.69	1	1	0.98
Ti3	0.0977	0.2557	0.3733	0.00544	0.01394	1.54	6.15	57.76	1	1	2.24
Ti4	0.3670	0.2498	0.1247	0.01609	0.01628	6.56	6.74	35.56	1	1	1.01
O1	0.6980	0.8128	0.2421	-0.00814	0.00362	1.66	-1.58	-52.90	1	1	-1.87
O2	0.9758	0.6910	-0.0088	0.00719	0.00222	-0.58	-0.81	41.79	1	1	1.26
O3	0.2194	0.1891	0.2410	0.00362	0.00190	-0.27	-0.64	51.02	1	1	1.75
O4	0.4440	0.3116	-0.0093	-0.01037	0.00144	2.24	-0.89	-23.40	1	1	-0.61
O5	0.8876	0.5307	0.3518	0.02746	-0.02158	-8.30	3.77	-26.80	1	1	-0.71
O6	0.1304	-0.0168	0.0979	0.02352	-0.02803	-5.15	3.78	-42.63	1	1	-1.30
O7	0.3762	0.4831	0.3456	0.02119	-0.03195	-4.43	4.93	-59.32	1	1	-2.38
O8	0.6378	0.0294	0.1000	0.02754	-0.02457	-8.59	5.22	-35.77	1	1	-1.02
O9	0.5488	0.5333	0.1308	-0.02147	0.02631	4.84	-4.83	-54.92	1	1	-2.01
O10	0.2898	0.9599	0.3780	-0.02645	0.02170	5.13	-4.54	-49.99	1	1	-1.69
O11	0.0448	0.4676	0.1279	-0.02367	0.02158	4.43	-2.66	-35.39	1	1	-1.00
O12	0.8008	0.0293	0.3814	-0.02041	0.02734	4.63	-2.73	-34.78	1	1	-0.98

<sup>a</sup> Displacements of atoms along the **a** ( $\Delta x$ ) and **c** ( $\Delta z$ ) axes; <sup>b</sup>  $x$  ( $p_a$ ) and  $z$  ( $p_c$ ) components of  $\mathbf{p}_{atom}$ ; <sup>c</sup> Angle of  $\mathbf{p}_{atom}$  with the **a**–**b** plane; <sup>d</sup> The direction of  $\alpha \mathbf{p}_{atom}$ .

**Table 6.** Structural parameters obtained by the DFT calculations for BNT–5%BT ( $E_{in-situ} = 0$  kV/cm) in the  $Pc$  cell. The following lattice parameters were used:  $a = 0.55306$  nm,  $b = 0.55037$  nm,  $c = 1.65152$  nm,  $\alpha = \gamma = 90.0000^\circ$ , and  $\beta = 70.2530^\circ$ . The  $P_s$  of  $64.6\text{ }\mu\text{C}/\text{cm}^2$  with its angle ( $\alpha_m$ ) of  $36.0^\circ$  is estimated.

Atom	x (-)	y (-)	z (-)	$\Delta x$ (nm) <sup>a</sup>	$\Delta z$ (nm) <sup>a</sup>	$p_a$ <sup>b</sup> ( $\mu\text{C}/\text{cm}^2$ )	$p_c$ <sup>b</sup> ( $\mu\text{C}/\text{cm}^2$ )	$\alpha p_{atom}$ <sup>c</sup> (deg)	[u]	u	v] <sup>d</sup>
Bi1	0.2739	0.7477	0.2565	0.03420	0.02729	8.61	8.46	34.76	1	1	0.98
Bi2	0.0222	0.2542	0.0074	0.03328	0.02880	9.20	8.56	33.65	1	1	0.94
Na1	0.4994	0.7495	0.0032	0.02066	0.02188	1.70	1.62	34.18	1	1	0.96
Na2	0.7472	0.2539	0.2528	0.01940	0.02112	1.53	1.70	37.28	1	1	1.08
Ti1	0.6232	0.7589	0.3731	0.01998	0.01334	8.31	4.67	23.98	1	1	0.63
Ti2	0.8635	0.7520	0.1220	0.01464	0.01165	4.66	3.79	30.98	1	1	0.85
Ti3	0.0979	0.2557	0.3731	0.00601	0.01344	1.76	5.90	55.97	1	1	2.09
Ti4	0.3688	0.2496	0.1246	0.01757	0.01595	7.18	6.62	33.49	1	1	0.94
O1	0.6960	0.8121	0.2422	-0.00887	0.00373	1.80	-1.64	-51.08	1	1	-1.75
O2	0.9750	0.6913	-0.0088	0.00716	0.00207	-0.57	-0.76	40.68	1	1	1.22
O3	0.2194	0.1894	0.2410	0.00406	0.00166	-0.31	-0.55	46.05	1	1	1.47
O4	0.4429	0.3104	-0.0092	-0.01058	0.00140	2.28	-0.88	-22.81	1	1	-0.59
O5	0.8864	0.5309	0.3521	0.02726	-0.02123	-8.23	3.72	-26.64	1	1	-0.71
O6	0.1289	-0.0165	0.0982	0.02313	-0.02769	-5.06	3.73	-42.74	1	1	-1.31
O7	0.3741	0.4837	0.3459	0.02048	-0.03148	-4.28	4.85	-59.92	1	1	-2.44
O8	0.6373	0.0297	0.1001	0.02781	-0.02452	-8.66	5.23	-35.55	1	1	-1.01
O9	0.5488	0.5326	0.1310	-0.02114	0.02637	4.77	-4.82	-55.30	1	1	-2.04
O10	0.2893	0.9609	0.3781	-0.02640	0.02163	5.12	-4.52	-49.84	1	1	-1.68
O11	0.0452	0.4690	0.1279	-0.02314	0.02126	4.32	-2.62	-35.70	1	1	-1.02
O12	0.8013	0.0287	0.3812	-0.01976	0.02680	4.48	-2.67	-35.16	1	1	-1.00

<sup>a</sup> Displacements of atoms along the **a** ( $\Delta x$ ) and **c** ( $\Delta z$ ) axes; <sup>b</sup> x ( $p_a$ ) and z ( $p_c$ ) components of  $\mathbf{p}_{atom}$ ; <sup>c</sup> Angle of  $\mathbf{p}_{atom}$  with the **a**–**b** plane; <sup>d</sup> The direction of  $\alpha \mathbf{p}_{atom}$ .

## 5. Conclusions

The intrinsic responses of unit-cell parameters and local atomic polarization to  $E_{in-situ}$  were investigated by high-energy SR-XRD analyses combined with density functional theory (DFT) calculations for the single crystals of BNT and BNT–5%BT. High-quality single crystals of BNT and BNT–5%BT grown by a high- $P_{O_2}$  TSSG method exhibited a  $P_r$  of 34–36  $\mu C/cm^2$  along  $<001>_{pc}$ , which quantitatively is in good agreement with the components of  $<001>_{pc}$  of the  $\mathbf{P}_s$  vectors estimated by the DFT calculations. The structural analyses provide direct evidence that the BNT and BNT–5%BT crystals have monoclinic  $Cc$  symmetry under an  $E_{in-situ}$  up to 70 kV/cm along  $<001>_{pc}$ . The BNT–5%BT crystals are found to exhibit a  $\mathbf{P}_s$  rotation by *ca.* 2° by an  $E_{in-situ}$  of 70 kV/cm along  $<001>_{pc}$  whereas the  $\mathbf{P}_s$  vector remains unchanged in the BNT crystals.

## Acknowledgments

The synchrotron radiation experiments were carried out with the approval of the Japan Synchrotron Radiation Research Institute (JASRI; Proposal Nos. 2011B1386, 2012A1359, and 2012B1243). This study was partly supported by a Grant-in-Aid for Research Fellows of the Japan Society for the Promotion of Science (No. 11J06837).

## Author Contributions

Masaru Miyayama and Yuji Noguchi initiated and supervised the project. Motohiro Ogino and Yuuki Kitanaka contributed to the crystal growth and analyzed the structural data. Yoshihiro Kuroiwa and Chikako Moriyoshi initiated work on *in-situ* SR-XRD measurements under electric fields. Motohiro Ogino and Yuji Noguchi suggested the principle idea and wrote the manuscript. Yuji Noguchi performed DFT calculations.

## Conflicts of Interest

The authors declare no conflict of interest.

## References

1. Shrout, T.R. Characteristics of relaxor-based piezoelectric single crystals for ultrasonic transducers. *IEEE Trans. Ultrason. Ferroelectr. Freq. Control* **1997**, *44*, 1140–1147.
2. Noheda, B.; Zhong, Z.; Cox, D.; Shirane, G.; Park, S.-E.; Rehrig, P. Electric-field-induced phase transitions in rhombohedral  $Pb(Zn_{1/3}Nb_{2/3})_{1-x}Ti_xO_3$ . *Phys. Rev. B* **2002**, *65*, doi: 10.1103/PhysRevB.65.224101.
3. Fu, H.; Cohen, R. Polarization rotation mechanism for ultrahigh electromechanical response in single-crystal piezoelectrics. *Nature* **2000**, *403*, 281–283.
4. Damjanovic, D. Comments on origins of enhanced piezoelectric properties in ferroelectrics. *IEEE Trans. Ultrason. Ferroelectr. Freq. Control* **2009**, *56*, 1574–1585.
5. Takenaka, T.; Maruyama, K.; Sakata, K.  $(Bi_{1/2}Na_{1/2})TiO_3$ -BaTiO<sub>3</sub> system for lead-free piezoelectric ceramics. *Jpn. J. Appl. Phys.* **1991**, *30*, 2236–2239.

6. Guo, Y.; Kakimoto, K.; Ohsato, H.  $(\text{Na}_{0.5}\text{K}_{0.5})\text{NbO}_3-\text{LiTaO}_3$  lead-free piezoelectric ceramics. *Mater. Lett.* **2005**, *59*, 241–244.
7. Maeder, M.D.; Damjanovic, D.; Setter, N. Lead free piezoelectric materials. *J. Electroceram.* **2004**, *13*, 385–392.
8. Nagata, H.; Yoshida, M.; Makiuchi, Y.; Takenaka, T. Large piezoelectric constant and high curie temperature of lead-free piezoelectric ceramic ternary system based on bismuth sodium titanate-bismuth potassium titanate-barium titanate near the morphotropic phase boundary. *Jpn. J. Appl. Phys.* **2003**, *42*, 7401–7403.
9. Shrout, T.R.; Zhang, S.J. Lead-free piezoelectric ceramics: Alternatives for PZT? *J. Electroceram.* **2007**, *19*, 113–126.
10. Vakhrushev, S.B.; Isupov, V.A.; Kvyatkovsky, B.E.; Okuneva, N.M.; Pronin, I.P.; Smolensky, G.A.; Syrnikov, P.P. Phase transitions and soft modes in sodium bismuth titanate. *Ferroelectrics* **1985**, *63*, 153–160.
11. Takenaka, T.; Sakata, K. Dielectric, piezoelectric and pyroelectric properties of  $(\text{BiNa})_{1/2}\text{TiO}_3$ -based ceramics. *Ferroelectrics* **1989**, *95*, 153–156.
12. Sasaki, A.; Chiba, T.; Mamiya, Y.; Otsuki, E. Dielectric and piezoelectric properties of  $(\text{Bi}_{0.5}\text{Na}_{0.5})\text{TiO}_3-(\text{Bi}_{0.5}\text{K}_{0.5})\text{TiO}_3$  systems. *Jpn. J. Appl. Phys.* **1999**, *38*, 5564–5567.
13. Roleder, K.; Franke, I.; Glazer, A.M.; Thomas, P.A.; Miga, S.; Suchanicz, J. The piezoelectric effect in  $\text{Na}_{0.5}\text{Bi}_{0.5}\text{TiO}_3$  ceramics. *J. Phys. Condens. Matter* **2002**, *14*, 5399–5406.
14. Jones, G.O.; Thomas, P.A. The tetragonal phase of  $\text{Na}_{0.5}\text{Bi}_{0.5}\text{TiO}_3$ —A new variant of the perovskite structure. *Acta Crystallogr. Sect. B Struct. Sci.* **2000**, *56*, 426–430.
15. Elkechai, O.; Manier, M.; Mercurio, J.P.  $\text{Na}_{0.5}\text{Bi}_{0.5}\text{TiO}_3-\text{K}_{0.5}\text{Bi}_{0.5}\text{TiO}_3$  (NBT-KBT) system: A structural and electrical study. *Phys. Status Solidi* **1996**, *157*, 499–506.
16. Kreisel, J.; Glazer, A.M.; Jones, G.; Thomas, P.A.; Abello, L.; Lucaleau, G. An X-ray diffraction and Raman spectroscopy investigation of A-site substituted perovskite compounds: The  $(\text{Na}_{1-x}\text{K}_x)_{0.5}\text{Bi}_{0.5}\text{TiO}_3$  ( $0 \leq x \leq 1$ ) solid solution. *J. Phys. Condens. Matter* **2000**, *12*, 3267–3280.
17. Jones, G.O.; Kreisel, J.; Jennings, V.; Geday, M.A.; Thomas, P.A.; Glazer, A.M. Investigation of a peculiar relaxor ferroelectric:  $\text{Na}_{0.5}\text{Bi}_{0.5}\text{TiO}_3$ . *Ferroelectrics* **2002**, *270*, 191–196.
18. Aleksandrova, I.P.; Sukhovsky, A.A.; Ivanov, Y.N.; Yablonskaya, Y.E.; Vakhrushev, S.B. Local and average structure of relaxor  $\text{Na}_{1/2}\text{Bi}_{1/2}\text{TiO}_3$  from the point of view of NMR. *Ferroelectrics* **2009**, *378*, 16–22.
19. Aksel, E.; Forrester, J.S.; Jones, J.L.; Thomas, P.A.; Page, K.; Suchomel, M.R. Monoclinic crystal structure of polycrystalline  $\text{Na}_{0.5}\text{Bi}_{0.5}\text{TiO}_3$ . *Appl. Phys. Lett.* **2011**, *98*, doi:10.1063/1.3573826.
20. Picht, G.; Töpfer, J.; Hennig, E. Structural properties of  $(\text{Bi}_{0.5}\text{Na}_{0.5})_{1-x}\text{Ba}_x\text{TiO}_3$  lead-free piezoelectric ceramics. *J. Eur. Ceram. Soc.* **2010**, *30*, 3445–3453.
21. Jones, G.O.; Thomas, P.A. Investigation of the structure and phase transitions in the novel A-site substituted distorted perovskite compound  $\text{Na}_{0.5}\text{Bi}_{0.5}\text{TiO}_3$ . *Acta Crystallogr. Sect. B Struct. Sci.* **2002**, *58*, 168–178.
22. Gorfman, S.; Glazer, A.M.; Noguchi, Y.; Miyayama, M.; Luo, H.; Thomas, P.A. Observation of a low-symmetry phase in  $\text{Na}_{0.5}\text{Bi}_{0.5}\text{TiO}_3$  crystals by optical birefringence microscopy. *J. Appl. Crystallogr.* **2012**, *45*, 444–452.

23. Chiang, Y.-M.; Farrey, G.W.; Soukhojak, A.N. Lead-free high-strain single-crystal piezoelectrics in the alkaline–bismuth–titane perovskite family. *Appl. Phys. Lett.* **1998**, *73*, doi:10.1063/1.122862.
24. Jo, W.; Daniels, J.E.; Jones, J.L.; Tan, X.; Thomas, P.A.; Damjanovic, D.; Rödel, J. Evolving morphotropic phase boundary in lead-free  $(\text{Bi}_{1/2}\text{Na}_{1/2})\text{TiO}_3$ – $\text{BaTiO}_3$  piezoceramics. *J. Appl. Phys.* **2011**, *109*, doi:10.1063/1.3530737.
25. Cernea, M.; Trupina, L.; Dragoi, C.; Vasile, B.S.; Trusca, R. Structural and piezoelectric characteristics of BNT–BT0.05 thin films processed by sol-gel technique. *J. Alloys Compd.* **2012**, *515*, 166–170.
26. Cordero, F.; Craciun, F.; Trequattrini, F.; Mercadelli, E.; Galassi, C. Phase transitions and phase diagram of the ferroelectric perovskite  $(\text{Na}_{0.5}\text{Bi}_{0.5})_{1-x}\text{Ba}_x\text{TiO}_3$  by anelastic and dielectric measurements. *Phys. Rev. B* **2010**, *81*, doi:10.1103/PhysRevB.81.144124.
27. Ma, C.; Guo, H.; Tan, X. A New Phase Boundary in  $(\text{Bi}_{1/2}\text{Na}_{1/2})\text{TiO}_3$ – $\text{BaTiO}_3$  Revealed via a Novel Method of Electron Diffraction Analysis. *Adv. Funct. Mater.* **2013**, *23*, 5261–5266.
28. Ma, C.; Guo, H.; Beckman, S.P.; Tan, X. Creation and destruction of morphotropic phase boundaries through electrical poling: A case study of lead-free  $(\text{Bi}_{1/2}\text{Na}_{1/2})\text{TiO}_3$ – $\text{BaTiO}_3$  piezoelectrics. *Phys. Rev. Lett.* **2012**, *109*, doi:10.1103/PhysRevLett.109.107602.
29. Yao, J.; Yan, L.; Ge, W.; Luo, L.; Li, J.; Viehland, D.; Zhang, Q.; Luo, H. Evolution of domain structures in  $\text{Na}_{1/2}\text{Bi}_{1/2}\text{TiO}_3$  single crystals with  $\text{BaTiO}_3$ . *Phys. Rev. B* **2011**, *83*, doi:10.1103/PhysRevB.83.054107.
30. Kling, J.; Tan, X.; Jo, W.; Kleebe, H.-J.; Fuess, H.; Rödel, J. *In situ* transmission electron microscopy of electric field-triggered reversible domain formation in bi-based lead-free piezoceramics. *J. Am. Ceram. Soc.* **2010**, *93*, 2452–2455.
31. Kreisel, J.; Glazer, A.M. Estimation of the compressibility of  $\text{Na}_{0.5}\text{Bi}_{0.5}\text{TiO}_3$  and related perovskite-type titanates. *J. Phys. Condens. Matter* **2000**, *12*, 9689–9698.
32. Kreisel, J.; Glazer, A.; Bouvier, P.; Lucaleau, G. High-pressure raman study of a relaxor ferroelectric: The  $\text{Na}_{0.5}\text{Bi}_{0.5}\text{TiO}_3$  perovskite. *Phys. Rev. B* **2001**, *63*, doi:10.1103/PhysRevB.63.174106.
33. Kreisel, J.; Bouvier, P.; Dkhil, B.; Thomas, P.; Glazer, A.; Welberry, T.; Chaabane, B.; Mezouar, M. High-pressure X-ray scattering of oxides with a nanoscale local structure: Application to  $\text{Na}_{1/2}\text{Bi}_{1/2}\text{TiO}_3$ . *Phys. Rev. B* **2003**, *68*, doi:10.1103/PhysRevB.68.014113.
34. Kreisel, J.; Bouvier, P.; Dkhil, B.; Chaabane, B.; Glazer, A.M.; Thomas, P.A.; Welberry, T.R. Effect of high pressure on the relaxor ferroelectrics  $\text{Na}_{1/2}\text{Bi}_{1/2}\text{TiO}_3$  (NBT) and  $\text{PbMg}_{1/3}\text{Nb}_{2/3}\text{O}_3$  (PMN). *Ferroelectrics* **2004**, *302*, 293–298.
35. Thomas, P.A.; Trujillo, S.; Boudard, M.; Gorfman, S.; Kreisel, J. Diffuse X-ray scattering in the lead-free piezoelectric crystals  $\text{Na}_{1/2}\text{Bi}_{1/2}\text{TiO}_3$  and Ba-doped  $\text{Na}_{1/2}\text{Bi}_{1/2}\text{TiO}_3$ . *Solid State Sci.* **2010**, *12*, 311–317.
36. Ge, W.; Cao, H.; Li, J.; Viehland, D.; Zhang, Q.; Luo, H. Influence of dc-bias on phase stability in Mn-doped  $\text{Na}_{0.5}\text{Bi}_{0.5}\text{TiO}_3$ –5.6 at.% $\text{BaTiO}_3$  single crystals. *Appl. Phys. Lett.* **2009**, *95*, doi:10.1063/1.3253412.
37. Daniels, J.E.; Jo, W.; Rödel, J.; Rytz, D.; Donner, W. Structural origins of relaxor behavior in a  $0.96(\text{Bi}_{1/2}\text{Na}_{1/2})\text{TiO}_3$ – $0.04\text{BaTiO}_3$  single crystal under electric field. *Appl. Phys. Lett.* **2011**, *98*, doi:10.1063/1.3602316.

38. Keeble, D.S.; Barney, E.R.; Keen, D.A.; Tucker, M.G.; Kreisel, J.; Thomas, P.A. Bifurcated polarization rotation in bismuth-based piezoelectrics. *Adv. Funct. Mater.* **2013**, *23*, 185–190.
39. Oh, T.; Kim, M.-H. Phase relation and dielectric properties in  $(\text{Bi}_{1/2}\text{Na}_{1/2})_{1-x}\text{Ba}_x\text{TiO}_3$  lead-free ceramics. *Mater. Sci. Eng. B Solid State Mater. Adv. Technol.* **2006**, *132*, 239–246.
40. Xu, C.; Lin, D.; Kwok, K.W. Structure, electrical properties and depolarization temperature of  $(\text{Bi}_{0.5}\text{Na}_{0.5})\text{TiO}_3\text{--BaTiO}_3$  lead-free piezoelectric ceramics. *Solid State Sci.* **2008**, *10*, 934–940.
41. Maurya, D.; Pramanick, A.; An, K.; Priya, S. Enhanced piezoelectricity and nature of electric-field induced structural phase transformation in textured lead-free piezoelectric  $\text{Na}_{0.5}\text{Bi}_{0.5}\text{TiO}_3\text{--BaTiO}_3$  ceramics. *Appl. Phys. Lett.* **2012**, *100*, doi:10.1063/1.4709404.
42. Rödel, J.; Jo, W.; Seifert, K.T.P.; Anton, E.-M.; Granzow, T.; Damjanovic, D. Perspective on the Development of Lead-free Piezoceramics. *J. Am. Ceram. Soc.* **2009**, *92*, 1153–1177.
43. Chen, M.; Xu, Q.; Kim, B.H.; Ahn, B.K.; Ko, J.H.; Kang, W.J.; Nam, O.J. Structure and electrical properties of  $(\text{Na}_{0.5}\text{Bi}_{0.5})_{1-x}\text{Ba}_x\text{TiO}_3$  piezoelectric ceramics. *J. Eur. Ceram. Soc.* **2008**, *28*, 843–849.
44. Roleder, K.; Suchanicz, J.; Kania, A. Time dependence of electric permittivity in  $\text{Na}_{0.5}\text{Bi}_{0.5}\text{TiO}_3$  single crystals. *Ferroelectrics* **1989**, *89*, 1–5.
45. Suchanicz, J.; Roleder, K.; Kania, A.; Hańderek, J. Electrostrictive strain and pyroeffect in the region of phase coexistence in  $\text{Na}_{0.5}\text{Bi}_{0.5}\text{TiO}_3$ . *Ferroelectrics* **1988**, *77*, 107–110.
46. Onozuka, H.; Kitanaka, Y.; Noguchi, Y.; Miyayama, M. Crystal Growth and characterization of  $(\text{Bi}_{0.5}\text{Na}_{0.5})\text{TiO}_3\text{--BaTiO}_3$  single crystals obtained by a top-seeded solution growth method under high-pressure oxygen atmosphere. *Jpn. J. Appl. Phys.* **2011**, *50*, doi:10.1143/JJAP.50.09NE07.
47. Kitanaka, Y.; Onozuka, H.; Noguchi, Y.; Miyayama, M. High-performance ferroelectric  $\text{Bi}_{0.5}\text{Na}_{0.5}\text{TiO}_3$  Single crystals grown by top-seeded solution growth method under high-pressure oxygen atmosphere. *Ferroelectrics* **2011**, *414*, 24–29.
48. Kitanaka, Y.; Noguchi, Y.; Miyayama, M. High-Performance ferroelectric  $\text{Bi}_4\text{Ti}_3\text{O}_{12}$  single crystals grown by top-seeded solution growth method under high-pressure oxygen atmosphere. *Jpn. J. Appl. Phys.* **2010**, *49*, doi:10.1143/JJAP.49.09MC06.
49. Hirano, K.; Onozuka, H.; Kitanaka, Y.; Noguchi, Y.; Miyayama, M. Leakage current and polarization properties of  $(\text{Bi}_{0.5}\text{Na}_{0.5})\text{TiO}_3\text{--BaTiO}_3$  single crystals. *Key Eng. Mater.* **2014**, *582*, 96–99.
50. Moriyoshi, C.; Hiramoto, S.; Ohkubo, H.; Kuroiwa, Y.; Osawa, H.; Sugimoto, K.; Kimura, S.; Takata, M.; Kitanaka, Y.; Noguchi, Y.; et al. Synchrotron Radiation study on time-resolved tetragonal lattice strain of  $\text{BaTiO}_3$  under electric field. *Jpn. J. Appl. Phys.* **2011**, *50*, doi:10.1143/JJAP.50.09NE05.
51. Kitanaka, Y.; Yanai, K.; Noguchi, Y.; Miyayama, M.; Kagawa, Y.; Moriyoshi, C.; Kuroiwa, Y. Non-180° polarization rotation of ferroelectric  $(\text{Bi}_{0.5}\text{Na}_{0.5})\text{TiO}_3$  single crystals under electric field. *Phys. Rev. B* **2014**, *89*, doi:10.1103/PhysRevB.89.104104.
52. Yanai, K.; Kitanaka, Y.; Noguchi, Y.; Miyayama, M.; Moriyoshi, C.; Kuroiwa, Y.; Kurushima, K.; Mori, S.; Kagawa, Y. Enhanced polarization switching in ferroelectric  $\text{Bi}_{0.5}\text{Na}_{0.5}\text{TiO}_3$  single crystals by defect control. *Phys. Status Solidi* **2013**, *443*, 791–795.
53. Kitanaka, Y.; Noguchi, Y.; Miyayama, M.; Kagawa, Y.; Moriyoshi, C.; Kuroiwa, Y. Synchrotron radiation analyses of domain switching and lattice strain behaviors for ferroelectric  $(\text{Bi}_{0.5}\text{Na}_{0.5})\text{TiO}_3$  single crystals under electric fields. *Ferroelectrics* **2013**, *443*, 1–7.

54. Zhang, Q.; Zhang, Y.; Wang, F.; Wang, Y.; Lin, D.; Zhao, X.; Luo, H.; Ge, W.; Viehland, D. Enhanced piezoelectric and ferroelectric properties in Mn-doped  $\text{Na}_{0.5}\text{Bi}_{0.5}\text{TiO}_3$ – $\text{BaTiO}_3$  single crystals. *Appl. Phys. Lett.* **2009**, *95*, doi:10.1063/1.3222942.
55. Aksel, E.; Forrester, J.S.; Nino, J.C.; Page, K.; Shoemaker, D.P.; Jones, J.L. Local atomic structure deviation from average structure of  $\text{Na}_{0.5}\text{Bi}_{0.5}\text{TiO}_3$ : Combined X-ray and neutron total scattering study. *Phys. Rev. B* **2013**, *87*, doi:10.1103/PhysRevB.87.104113.
56. Langreth, D.; Perdew, J. Theory of nonuniform electronic systems. I. Analysis of the gradient approximation and a generalization that works. *Phys. Rev. B* **1980**, *21*, 5469–5493.
57. Blöchl, P.E. Projector augmented-wave method. *Phys. Rev. B* **1994**, *50*, 17953–17979.
58. Perdew, J.; Ruzsinszky, A.; Csonka, G.; Vydrov, O.; Scuseria, G.; Constantin, L.; Zhou, X.; Burke, K. Restoring the density-gradient expansion for exchange in solids and surfaces. *Phys. Rev. Lett.* **2008**, *100*, doi:10.1103/PhysRevLett.100.136406.
59. Grüning, M.; Marini, A.; Gonze, X. Implementation and testing of Lanczos-based algorithms for random-phase approximation eigenproblems. *Comput. Mater. Sci.* **2011**, *50*, 2148–2156.
60. Glazer, A.M. The classification of tilted octahedra in perovskites. *Acta Crystallogr. Sect. B Struct. Crystallogr. Cryst. Chem.* **1972**, *28*, 3384–3392.
61. Stokes, H.T.; Kisi, E.H.; Hatch, D.M.; Howard, C.J. Group-theoretical analysis of octahedral tilting in ferroelectric perovskites. *Acta Crystallogr. Sect. B Struct. Sci.* **2002**, *58*, 934–938.
62. Bubesh Babu, J.; He, M.; Zhang, D.F.; Chen, X.L.; Dhanasekaran, R. Enhancement of ferroelectric properties of  $\text{Na}_{1/2}\text{Bi}_{1/2}\text{TiO}_3$ – $\text{BaTiO}_3$  single crystals by Ce dopings. *Appl. Phys. Lett.* **2007**, *90*, doi:10.1063/1.2709917.
63. Ge, W.; Liu, H.; Zhao, X.; Fang, B.; Li, X.; Wang, F.; Zhou, D.; Yu, P.; Pan, X.; Lin, D.; et al. Crystal growth and high piezoelectric performance of  $0.95\text{Na}_{0.5}\text{Bi}_{0.5}\text{TiO}_3$ – $0.05\text{BaTiO}_3$  lead-free ferroelectric materials. *J. Phys. D Appl. Phys.* **2008**, *41*, doi:10.1088/0022-3727/41/11/115403.
64. Suzuki, M.; Morishita, A.; Kitanaka, Y.; Noguchi, Y.; Miyayama, M. Polarization and piezoelectric properties of high performance bismuth sodium titanate single crystals grown by high-oxygen-pressure flux method. *Jpn. J. Appl. Phys.* **2010**, *49*, doi:10.1143/JJAP.49.09MD09.
65. Bethe, K.; Welz, F. Preparation and properties of  $(\text{Ba},\text{Sr})\text{TiO}_3$  single crystals. *Mater. Res. Bull.* **1971**, *6*, 209–217.
66. Bell, A.J. Phenomenologically derived electric field-temperature phase diagrams and piezoelectric coefficients for single crystal barium titanate under fields along different axes. *J. Appl. Phys.* **2001**, *89*, doi:10.1063/1.1352682.
67. Li, Y.L.; Cross, L.E.; Chen, L.Q. A phenomenological thermodynamic potential for  $\text{BaTiO}_3$  single crystals. *J. Appl. Phys.* **2005**, *98*, doi:10.1063/1.2042528.
68. Uesu, Y.; Matsuda, M.; Yamada, Y.; Fujishiro, K.; Cox, D.E.; Noheda, B.; Shirane, G. Symmetry of high-piezoelectric pb-based complex perovskites at the morphotropic phase boundary: I. Neutron diffraction study on  $\text{Pb}(\text{Zn}_{1/3}\text{Nb}_{2/3})\text{O}_3$ –9% $\text{PbTiO}_3$ . *J. Phys. Soc. Jpn.* **2002**, *71*, 960–965.
69. Yamada, Y.; Uesu, Y.; Matsuda, M.; Fujishiro, K.; Cox, D.E.; Noheda, B.; Shirane, G. Symmetry of high-piezoelectric pb based complex perovskites at the morphotropic phase boundary: II. Theoretical treatment. *J. Phys. Soc. Jpn.* **2002**, *71*, 966–970.

70. Ohwada, K.; Hirota, K.; Rehrig, P.; Fujii, Y.; Shirane, G. Neutron diffraction study of field-cooling effects on the relaxor ferroelectric  $\text{Pb}[(\text{Zn}_{1/3}\text{Nb}_{2/3})_{0.92}\text{Ti}_{0.08}]\text{O}_3$ . *Phys. Rev. B* **2003**, *67*, doi:10.1103/PhysRevB.67.094111.
71. Rajan, K.K.; Shanthi, M.; Chang, W.S.; Jin, J.; Lim, L.C. Dielectric and piezoelectric properties of [001] and [011]-poled relaxor ferroelectric PZN–PT and PMN–PT single crystals. *Sens. Actuators A Phys.* **2007**, *133*, 110–116.
72. Brown, I.D.; Altermatt, D. Bond-valence parameters obtained from a systematic analysis of the Inorganic Crystal Structure Database. *Acta Crystallogr. Sect. B Struct. Sci.* **1985**, *41*, 244–247.
73. Sayers, D.; Stern, E.; Lytle, F. New Technique for Investigating noncrystalline structures: Fourier analysis of the extended X-ray—Absorption fine structure. *Phys. Rev. Lett.* **1971**, *27*, 1204–1207.
74. Zhao, X.; Vanderbilt, D. Phonons and lattice dielectric properties of zirconia. *Phys. Rev. B* **2002**, *65*, doi:10.1103/PhysRevB.65.075105.
75. Zhong, W.; Vanderbilt, D. Phase transitions in  $\text{BaTiO}_3$  from first principles. *Phys. Rev. Lett.* **1994**, *73*, 1861–1864.
76. Bagayoko, D.; Zhao, G.L.; Fan, J.D.; Wang, J.T. *Ab initio* calculations of the electronic structure and optical properties of ferroelectric tetragonal. *J. Phys. Condens. Matter* **1998**, *10*, 5645–5655.
77. Gou, G.Y.; Bennett, J.W.; Takenaka, H.; Rappe, A.M. Post density functional theoretical studies of highly polar semiconductive  $\text{Pb}(\text{Ti}_{1-x}\text{Ni}_x)\text{O}_{3-x}$  solid solutions: Effects of cation arrangement on band gap. *Phys. Rev. B* **2011**, *83*, doi:10.1103/PhysRevB.83.205115.
78. Miyazawa, H.; Natori, E.; Miyashita, S.; Shimoda, T.; Ishii, F.; Oguchi, T. Electronic states of perovskite-type oxides and ferroelectricity. *Jpn. J. Appl. Phys.* **2000**, *39*, 5679–5682.
79. Kitanaka, Y.; Ogino, M.; Hirano, K.; Noguchi, Y.; Miyayama, M.; Kagawa, Y.; Moriyoshi, C.; Kuroiwa, Y.; Torii, S.; Kamiyama, T. Crystal Structural analyses of ferrielectric tetragonal  $(\text{Bi}_{1/2}\text{Na}_{1/2})\text{TiO}_3$ –7% $\text{BaTiO}_3$  powders and single crystals. *Jpn. J. Appl. Phys.* **2013**, *52*, doi:10.7567/JJAP.52.09KD01.

© 2014 by the authors; licensee MDPI, Basel, Switzerland. This article is an open access article distributed under the terms and conditions of the Creative Commons Attribution license (<http://creativecommons.org/licenses/by/3.0/>).